JOURNAL OF AIRCRAFT
Vol. 40, No. 4, July–August 2003

Boundary Condition for Simulation of Flow Over Porous Surfaces

Neal T. Frink,[*] Daryl L. Bonhaus,[†] Veer N. Vatsa,[‡] and Steven X. S. Bauer[*]
NASA Langley Research Center, Hampton, Virginia, 23681
and
Ana F. Tinetti[§]
NCI Information Systems, Hampton, Virginia 23681

A new boundary condition is presented for simulating the flow over passively porous surfaces. The model eliminates the need for construction of a grid within an underlying plenum, thereby simplifying the numerical modeling of passively porous flow control systems and reducing computation cost. Two structured-grid flow solvers, TLNS3D and CFL3D, and one unstructured solver, USM3Dns, are used to develop and evaluate the model. Results presented for the three codes on a slender forebody with circumferential porosity and on a wing with leading edge porosity demonstrate good agreement with experimental data and a remarkable ability to predict the aggregate aerodynamic effects of surface porosity with a simple boundary condition.

Nomenclature

A = area
a = speed of sound
b = wingspan
C_D = drag force coefficient
C_L = lift force coefficient
C_p = pressure coefficient
c = wing chord
c_1 = magnification parameter
c_2 = relaxation parameter
D = model base diameter
L/D = lift-to-drag ratio
M = Mach number
$\bar{m}$ = area averaged mass flux
N_{porous} = number of cell faces on porous boundary
p = pressure
Re = Reynolds number
s = solidity parameter, A_{solid}/A_1
T = temperature
u = local velocity normal to porous surface
x, y, z = cartesian coordinates
y = spanwise distance
α = angle of attack, deg
γ = ratio of specific heats for air, 1.4
ρ = density
φ = contraction coefficient, or circumferential station on slender body, 0 and 360 deg, windward and 180 deg, leeward

Subscripts

avg = averaged over surface
b = boundary
c = wing reference chord
D = model base reference diameter
domain = computational domain
effective = constricted orifice area
max = maximum
min = minimum
n = iteration number
normal = perpendicular to porous surface
porous = region of surface porosity
solid = solid region of porous surface
t = total stagnation quantity
tangent = tangent to porous surface
update = iterative update quantity
1 = upstream flow on porous surface
2 = minimum area of flow through porous surface
3 = downstream, fully mixed flow through porous surface
∞ = freestream condition

Introduction

PASSIVE porosity technology (PassPorT)[1] is an enabling flow alteration concept that can potentially resolve many aerodynamic problems. Its underlying principle is illustrated in the upper part of Fig. 1, which depicts a porous skin positioned over a closed cavity/plenum region. Local pressure differences within flow over the outer surface "communicate" through the plenum in concert with small amounts of mass transfer in and out of the porous surface, to alter its effective aerodynamic shape. For a properly designed system, the hole size is small with respect to the boundary-layer thickness and is less than or equal to the skin thickness. The flow velocity into and out of the plenum is low. PassPorT was originally applied to transonic airfoils to reduce the normal shock strength and, thus, eliminate shock-induced separation and lower the drag levels.[2–6]

More recently, the concept was applied to a supersonic delta wing to reduce the crossflow, shock-induced separation.[7] During this study, it was discovered that the connection of the plenum to high- and low-pressure regions on the wing, as shown in the middle of Fig. 1, allowed for localized "lift dumping," thus, providing roll and yaw control. Subsequent applications were envisioned such as conformal control effectors on military aircraft, as illustrated in the lower half of Fig. 1. The potential for broad application of this technology to aerodynamic concepts provided enough incentive to fund the fabrication of several porous models.

A family of four tangent-ogive forebodies was built (two 2.5 caliber and two 5.0 caliber, where each slenderness ratio consisted of one solid and one with 22% porosity surface). These models were extensively tested in the NASA Langley Research Center (LaRC) 7- by 10-Foot High Speed Wind Tunnel, 14 by 22-Foot Subsonic

---

Presented as Paper 2001-2412 at the 19th Applied Aerodynamics Conference, Anaheim, CA, 11 June 2001; received 6 February 2002; revision received 13 March 2003; accepted for publication 13 March 2003.

[*] Senior Research Engineer, Configuration Aerodynamics Branch Aerodynamics, Aerothermodynamics, and Acoustics Competency. Associate Fellow AIAA.

[†] Currently Principle Software Engineer, Symantec Research Laboratories, Symantec Corporation, 1 Symantec Way, Newport News, VA 23606.

[‡] Senior Research Scientist. Senior Member AIAA.

[§] Staff Engineer. Senior Member AIAA.

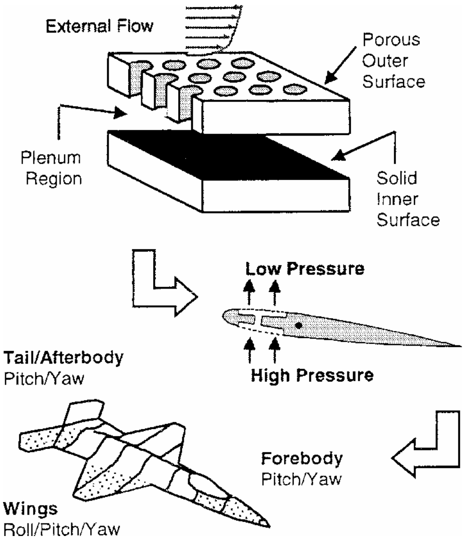

Fig. 1 PassPorT concept and application as conformal control effector on military aircraft.

Wind Tunnel, and Unitary Plan Wind Tunnel. In addition, the 5.0-caliber porous model was tested in the McDonnell Douglas Shear Flow Facility. The results from these tests[8,9] showed that passive porous systems could be used to eliminate the asymmetric loading conditions that occur at high angles of attack on axisymmetric slender bodies, even at a zero sideslip angle. This side force is a result of asymmetric pressure loading caused by differences in the location of the separation-induced vortex on either side of the forebody. This phenomenon has been documented extensively.[10–13] Numerous studies have been conducted to develop devices that eliminate or minimize the asymmetric behavior of forebodies.[14–17] These fixes typically involve reshaping the nose or adding devices, such as strakes, to the existing geometry that add weight and are beneficial for only a limited range of conditions. In Refs. 8 and 9, a passive porous system was investigated to alleviate the asymmetric loading on the forebody. These tests also showed that pitch and yaw control could be attained by opening or closing the porous surface on one side or the other on the forebodies.

A zero-sweep, porous, General Aviation (Whitcomb)-1 [GA(W)-1][18] wing model was built and tested in the NASA LaRC 14- by 22-Foot Subsonic Wind Tunnel. All surfaces on the model were constructed with porosity that could be closed by covering the holes with tape. Through selective opening and closing of porous regions, the locations on the wing that induced the most pitch, yaw, and roll control were identified, as were the locations responsible for either increased performance (i.e., increased $L/D_{\max}$ and angle of attack at which $L/D_{\max}$ occurs) or increased drag. This model was later reskinned and modified to include actuators inside the plenums to open and close the porous surfaces. The results showed that no pressure lag occurred. The recorded forces responded as quickly as the porous surface could be actuated, indicating no appreciable lag due to pressure equalization.

With the success achieved in the wind-tunnel tests, a series of research efforts were conducted to develop computational fluid dynamics (CFD) models to represent a passive porous system. The first studies utilized Darcy's law (see Ref. 19). These had limited success and were fairly accurate, as long as the coefficient required in the equation was chosen correctly. Later attempts with modified versions of Darcy's law and to utilize some techniques used by researchers to determine oxygen transport through capillary walls were slightly more successful (see Ref. 20).

The work presented in this paper builds on a methodology first developed by McDonnell Douglas to simulate normal flow through a screen positioned at a zonal-grid interface boundary.[21] The primary contribution of this work is to reformulate that approach into a new boundary condition for simulation of the flow over porous aerodynamic surfaces. This eliminates the need for construction of a grid within an underlying plenum, thereby simplifying the numerical modeling of passively porous flow control systems and reducing computation cost. Code experts for two structured-grid flow solvers, TLNS3D and CFL3D, and one unstructured solver, USM3Dns, collaborated with an experimental porosity expert to develop the model and implement it into their respective codes. This paper describes the formulation of the new boundary condition and presents an assessment of its effectiveness in simulating the aggregate aerodynamics induced by surface porosity by the use of wind-tunnel results for a 5.0-caliber tangent-ogive body and GA(W)-1 wing model. This technique was recently utilized in a passive porosity control effector design study[1] on the military aircraft configuration in Fig. 1.

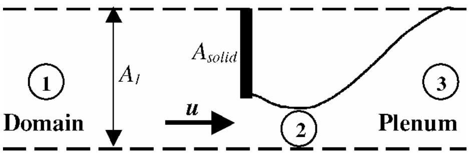

Fig. 2 Crosscut schematic of porous surface.

Porous Surface Flow Model

The proposed porous surface flow model builds on the general approach of Bush.[21] The Bush model was derived to pass flow information across a conterminous boundary separating an external computational grid zone from an internal plenum grid zone. The present approach is formulated as a surface boundary condition, thus eliminating the need for grid cells on the plenum side of a porous surface.

Figure 2 is a schematic of the porous surface model as a cut through a section of solid surface and a hole. Porosity is defined by a solidity parameter $s = A_{\text{solid}}/A_1$ that quantifies the area ratio between solid and total surface. Three uniform states are assumed across the porous surface: 1) upstream, 2) minimum area, and 3) downstream (fully mixed). The upstream and downstream areas are equal ($A_1 = A_3$). The area at 2 is assumed to be reduced by the solidity parameter s and a contraction coefficient that represents a further area reduction due to flow through the orifice, $A_2 = A_1\varphi(1 - s)$ where ($\varphi = A_{\text{effective}}/A_1$). The contraction coefficient in Ref. 21 is determined from curve fits to experimental data following guidelines provided by Cornell[22] and Rouse[23]:

$$\varphi_o = 0.04137/[1.0982 - (1 - s)] + 0.57293 + 0.005786(1 - s)$$

$$\varphi = \varphi_o + 0.185 s^{\frac{1}{4}}(p_{t2}/p_2 - 1)$$

Governing Equations

The governing equations are derived from conservation of mass and momentum (normal to the surface) for steady, one-dimensional, isentropic flow of a perfect gas. Density and velocity are nondimensionalized by freestream density ρ_∞ and speed of sound a_∞, respectively; pressure by $\rho_\infty a_\infty^2$; and temperature by static freesteam temperature T_∞. It is also assumed that the flow is adiabatic, that is, no heat transfer, and that there is no total pressure loss during jet formation. The latter assumption is valid as long as the fluid passing through the orifice has an inviscid core. Thus, the flow normal to the porous surface boundary is determined by the following equations. Conservation of mass from 1–2 is

$$(\rho u)_1 = (\rho u)_2\varphi(1 - s) \tag{1}$$

Conservation of mass from 1–3 is

$$(\rho u)_1 = (\rho u)_3 \tag{2}$$

No loss in jet formation from 1–2 is

$$p_{t1} = p_{t2} \tag{3}$$

Momentum balance from 2–3 with induced screen losses is

$$p_2\left[1 + \gamma M_2^2\varphi(1 - s)\right] = p_3\left(1 + \gamma M_3^2\right) \tag{4}$$

Auxiliary isentropic flow relations are

$$(\rho u) = \left(\gamma / \sqrt{T_t}\right) p M \left\{1 + [(\gamma - 1)/2] M^2\right\}^{\frac{1}{2}} \tag{5}$$

$$p_t = p\left\{1 + [(\gamma - 1)/2] M^2\right\}^{\gamma/(\gamma - 1)} \tag{6}$$

Under the assumption that a tangential pressure gradient exists across the surface and the net mass flux across a passively porous surface is zero, there will always be some flow transversing both into and out of the plenum at any given time. Thus, the application of the governing equations is dependent on the direction of the surface normal flow, which is a function of the local pressure gradient between the plenum and the domain. Formulations are presented hereafter for the two conditions.

Implementation

A general assumption for the present model is that entire process from state 1 to 3 in Fig. 2 transpires over an infinitesimal distance. Hence, the application of the model is in the form of a surface boundary condition. The following will describe the proposed boundary condition for flow moving both into ($p_{\text{plenum}} < p_{\text{domain}}$) and out of ($p_{\text{plenum}} > p_{\text{domain}}$) the plenum. The local velocity u is defined as the component normal to the surface.

Flow Into Plenum: ($p_{\text{plenum}} < p_{\text{domain}}$)

The configuration for flow into the plenum from the domain is presented in Fig. 2. The first step is to assume choked flow by the assumption that $M_2^2 = 1$ and to solve Eq. (1) with Eq. (5) written at state 3 and Eq. (4) for M_3^2 via Newton iteration

$$\frac{\gamma + 1}{2}\left[\frac{1 + \gamma M_3^2}{1 + \gamma \varphi(1 - s)}\right]^2 \varphi^2 (1 - s)^2 - M_3^2 \left(1 + \frac{\gamma - 1}{2} M_3^2\right) = 0 \tag{7}$$

From this result, the maximum mass flow is computed with Eq. (5) written at state 3

$$(\rho u)_{\max} = \left(\gamma / \sqrt{T_t}\right) p_3 M_3 \left\{1 + [(\gamma - 1)/2] M_3^2\right\}^{\frac{1}{2}} \tag{8}$$

If $(\rho u)_1 \leq (\rho u)_{\max}$, that is, not choked, then we first solve Eq. (2) with Eq. (5) written at state 3 for M_3^2:

$$M_3^2 = \frac{-1 + \sqrt{1 + 2[(\gamma - 1)/\gamma^2] T_t (\rho u)_1^2 / p_3^2}}{(\gamma - 1)} \tag{9}$$

and then solve Eq. (1) with Eq. (5) written at state 2 and Eq. (4) for M_2^2 via Newton iteration:

$$M_2^2 \left(1 + \frac{\gamma - 1}{2} M_2^2\right)\left[\frac{1 + \gamma M_3^2}{1 + \gamma M_2^2 \varphi(1 - s)}\right]^2 \varphi^2 (1 - s)^2 - \frac{T_t}{\gamma^2} \frac{(\rho u)_1^2}{p_3^2} = 0 \tag{10}$$

If flow is choked, $(\rho u)_1 > (\rho u)_{\max}$, then we set $(\rho u)_1 = (\rho u)_{\max}$ and $M_2^2 = 1$. Now Eqs. (3) and (4) are used with Eq. (6) written at state 2 to compute p_{t1}:

$$p_{t1} = p_3 \frac{1 + \gamma M_3^2}{1 + \gamma M_2^2 \varphi(1 - s)} \left(1 + \frac{\gamma - 1}{2} M_2^2\right)^{\gamma/(\gamma - 1)} \tag{11}$$

M_1^2 is then computed with Eq. (5) written at state 1 via Newton iteration:

$$M_1^2 \left\{1 + [(\gamma - 1)/2] M_1^2\right\}^{-[(\gamma + 1)/(\gamma - 1)]} - \left(T_t / \gamma^2\right)\left[(\rho u)_1^2 / p_{t1}^2\right] = 0 \tag{12}$$

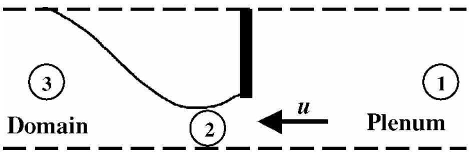

Fig. 3 Model for flow leaving plenum.

The boundary flux can now be computed with $(\rho u)_1$, M_1^2, and p_{t1}:

$$p_b = p_{t1}\left\{1 + [(\gamma - 1)/2] M_1^2\right\}^{-[\gamma/(\gamma - 1)]}$$

$$\rho_b = (\gamma p_b / T_t)\left\{1 + [(\gamma - 1)/2] M_1^2\right\}$$

$$u_{b,\text{normal}} = (\rho u)_1 / \rho_b$$

Note that $u_{b,\text{tangent}}$ is zero for a viscous boundary or the inviscid tangential velocity for an inviscid boundary.

Flow Leaving Plenum: ($p_{\text{plenum}} > p_{\text{domain}}$)

The configuration for flow into the domain from the plenum is presented in Fig. 3. The first step is to once again check for choked flow under the assumption that $M_2^2 = 1$. Equation (1) is then solved by the use of Eq. (5) written at state 1 and Eq. (3) for M_1^2 via Newton iteration:

$$\left([2/(\gamma + 1)]\left\{1 + [(\gamma - 1)/2] M_1^2\right\}\right)^{(\gamma + 1)/(\gamma - 1)} \times \varphi^2 (1 - s)^2 - M_1^2 = 0 \tag{13}$$

From this result, the maximum mass flow is computed with Eq. (5) written at state 1:

$$(\rho u)_{\max} = \left(\gamma / \sqrt{T_1}\right) p_1 M_1 \left\{1 + [(\gamma - 1)/2] M_1^2\right\}^{\frac{1}{2}} \tag{14}$$

If $(\rho u)_3 \leq (\rho u)_{\max}$, that is, not choked, then we solve Eq. (2) with Eq. (5) written at state 1 for M_1^2:

$$M_1^2 = \frac{-1 + \sqrt{1 + 2[(\gamma - 1)/\gamma^2] T_t \left[(\rho u)_3^2 / p_1^2\right]}}{(\gamma - 1)} \tag{15}$$

We then solve Eq. (1) with Eq. (5) written at state 2, as well as Eq. (3) for M_2^2 via Newton iteration:

$$\left\{1 + [(\gamma - 1)/2] M_1^2\right\}^{2\gamma/(\gamma - 1)} M_2^2 \left\{1 + [(\gamma - 1)/2] M_2^2\right\}^{-[(\gamma + 1)/(\gamma - 1)]} \times \varphi^2 (1 - s)^2 - \left(T_t / \gamma^2\right)\left[(\rho u)_3^2 / p_1^2\right] = 0 \tag{16}$$

If the flow is choked, $(\rho u)_3 > (\rho u)_{\max}$, we then set $(\rho u)_3 = (\rho u)_{\max}$ and $M_2^2 = 1$. Equations (3) and (6) can be used to compute pressure at state 2:

$$p_2 = p_1 \left\{\frac{1 + [(\gamma - 1)/2] M_1^2}{1 + [(\gamma - 1)/2] M_2^2}\right\}^{\gamma/(\gamma - 1)} \tag{17}$$

Equation (2) is then solved with Eq. (5) written at state 3 for M_3,

$$M_3^2 \left(1 + \frac{\gamma - 1}{2} M_3^2\right)\left[\frac{1 + \gamma M_2^2 \varphi(1 - s)}{1 + \gamma M_3^2}\right]^2 - \frac{T_t}{\gamma^2} \frac{(\rho u)_3^2}{p_2^2} = 0 \tag{18}$$

Finally, Eq. (6) written at state 3 and Eq. (4) are used to compute p_{t3}:

$$p_{t3} = p_2 \frac{1 + \gamma M_2^2 \varphi(1 - s)}{1 + \gamma M_3^2} \left(1 + \frac{\gamma - 1}{2} M_3^2\right)^{\gamma/(\gamma - 1)} \tag{19}$$

The boundary flux using $(\rho u)_3$, M_3^2, and p_{t3} are then given as

$$p_b = p_{t3}\left\{1 + [(\gamma - 1)/2]M_3^2\right\}^{-[\gamma/(\gamma - 1)]}$$

$$\rho_b = (\gamma p_b/T_t)\left\{1 + [(\gamma - 1)/2]M_3^2\right\}$$

$$u_{b,\mathrm{normal}} = (\rho u)_3/\rho_b$$

Note that $u_{b,\mathrm{tangent}}$ is zero for a viscous boundary or the inviscid tangential velocity for an inviscid boundary.

Determination of Plenum Pressure

A plenum pressure that yields a zero net mass flux balance across the porous surface must be determined. This pressure is used for p_3 in Eqs. (8–11) and for p_1 in Eqs. (14–17). The following describes an iterative procedure for the estimation of plenum pressure.

First an area-averaged pressure and normal mass flux over the porous surface are computed:

$$p_{\mathrm{avg}} = \frac{\sum_{i=1}^{N_{\mathrm{porous}}}(pA)_i}{\sum_{i=1}^{N_{\mathrm{porous}}}A_i}, \qquad \bar{m}_{\mathrm{porous}} = \frac{\sum_{i=1}^{N_{\mathrm{porous}}}(\rho uA)_i}{\sum_{i=1}^{N_{\mathrm{porous}}}A_i}$$

The initial value of plenum pressure is assumed to be the averaged pressure ($p_{\mathrm{plenum},1} = p_{\mathrm{avg}}$).

In the second iteration, a bracketed update to plenum pressure is computed:

$$p_{\mathrm{update}} = \min[(1 + c_1\bar{m}_{\mathrm{porous}})p_{\mathrm{plenum},n-1}, p_{t,\infty}]$$

$$p_{\mathrm{update}} = \max(p_{\mathrm{update}}, 1.005p_{\mathrm{min}})$$

where $c_1 = 10$ is a magnification parameter, and p_{min} is the minimum value of pressure on the porous surface from summation for p_{avg}.

It is necessary to impose a filter on the pressure updates to damp the temporal oscillations:

$$p_{\mathrm{plenum},n} = (c_2 p_{\mathrm{plenum},n-1} + p_{\mathrm{update}})/(c_2 + 1)$$

where the relaxation parameter $c_2 = 50$.

Description of Flow Solvers

The porous boundary condition has been implemented in two structured-grid flow solvers, TLNS3D and CFL3D, and one unstructured solver, USM3Dns. A brief description of the salient features of each code is included hereafter.

TLNS3D

The TLNS3D code[24,25] uses a cell-centered, finite volume approach for solving inviscid and viscous flows over complex configurations on general multiblock structured grids. A suite of algebraic and one- and two equation turbulence models is used for simulating turbulent flows. Artificial dissipation is added to the central-difference scheme for stability. TLNS3D also makes use of local time stepping, implicit residual smoothing, and multigrid techniques, in conjunction with a multistage Runge–Kutta time-stepping scheme to accelerate the convergence of the code to steady-state solutions.

CFL3D

CFL3D[26] solves the three-dimensional, time-dependent, thin-layer approximation to the Reynolds-averaged Navier–Stokes (RANS) equations using a finite volume formulation in generalized coordinates. It uses upwind-biased spatial differencing with Roe's[27] flux-difference splitting or Van Leer's[28] flux-vector splitting methods for the inviscid terms and central differences for the viscous and heat transfer terms. The code, which is second-order accurate in space, is advanced in time with an implicit three-factor approximate factorization (AF) scheme. Temporal subiterations with multigrid are used to recover time accuracy lost as a result of the AF approach during unsteady calculations. The code includes several grid connection strategies; a vast array of zero-, one-, and two-equation turbulence models (linear as well as nonlinear); and numerous boundary conditions. The results presented in this paper were obtained with the two equation k–ω shear-stress transport (SST) model of Menter.[29]

USM3Dns

USM3Dns[30] is a tetrahedral cell-centered, finite volume Euler and Navier–Stokes flow solver. Inviscid flux quantities are computed across each cell face with Roe's[27] flux-difference splitting. Spatial discretization is accomplished by a novel reconstruction process that is based on an analytical formulation for computing solution gradients within tetrahedral cells. The solution is advanced to a steady-state condition by an implicit backward-Euler time-stepping scheme. Flow turbulence effects are modeled by the Spalart–Allmaras one-equation turbulence model.[31] The model can be integrated all of the way to the wall, or can be coupled with a wall function to reduce the number of cells in the sublayer.

Results and Discussion

An assessment of the new porous boundary condition is made with two selected examples that use the three flow solvers. The first is a 5.0-caliber tangent ogive with and without forebody porosity. Without porosity, the forebody develops strong vortex asymmetries at high angles of attack that generate severe yawing moments. Surface porosity alleviates these asymmetries.

The second case is the GA(W)-1 with and without leading-edge porosity. The effect of the porosity is to reduce lift and increase drag. Such porosity is conceived as a conformal control device when applied asymmetrically to a wing to generate rolling and yawing moments.

5.0-Caliber Tangent-Ogive Forebody

A 5.0-caliber tangent-ogive forebody was tested, as one of a family of ogives, in the Langley 7 × 10 Foot High-Speed Wind Tunnel to investigate the effect of fineness ratio on the asymmetric loading of slender forebodies and the effectiveness of passive porosity in alleviating these asymmetries.[9] Figure 4 presents a full surface representation of the forebody. The original sting-mounted wind-tunnel model is 30 in. (76.2 cm) long and 4 in. (10.16 cm) in diameter. For the computational geometry depicted in Fig. 4, the sting has been removed and the body extended to 40 in. (101.6 m) in length, where it is terminated at an outflow boundary. This modification had a negligible impact on the forebody flow. Surface porosity is applied to the darkened region that extends from $x = 1$ to 20 in. (2.54 to 50.8 cm).

The computation of asymmetric vortex flows on slender ogive bodies at high angles of attack presents a challenging problem[32,33] that is beyond the scope of this paper. Such flows are characterized by massive crossflow separation with asymmetric feedback through the boundary layer and are highly sensitive to laminar-to-turbulent transition location, turbulence models, and numerical discretization. The present work is focused on the formulation and verification of

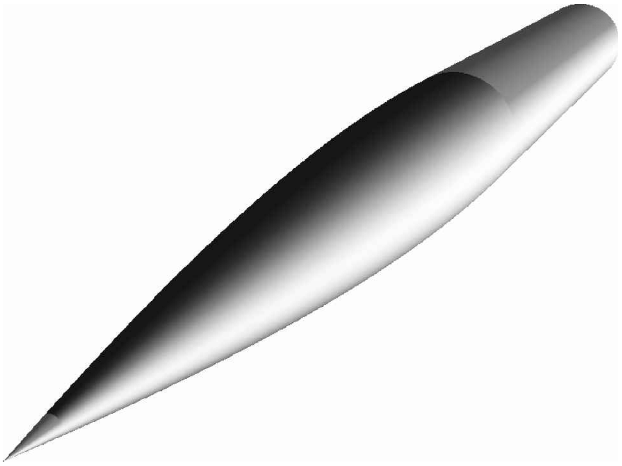

Fig. 4 Surface representation of 5.0-caliber tangent-ogive configuration; porous region denoted by shading.

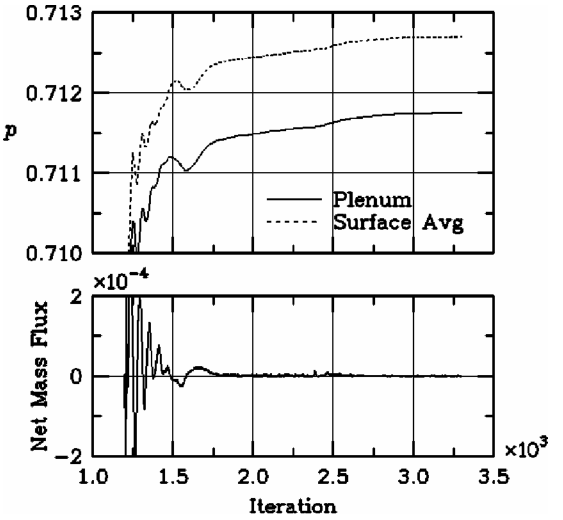

Fig. 5 Convergence of the net mass flux and the plenum and surface averaged pressures over the porous region of 5.0-caliber tangent-ogive forebody from USM3Dns: $M_\infty = 0.2$, $\alpha = 30$ deg, and $Re_D = 4 \times 10^5$.

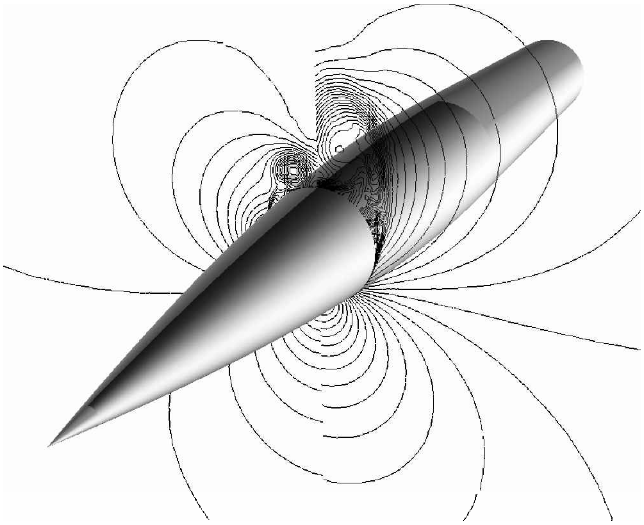

Fig. 6 Contours of density at $x/D = 2.5$. (solid surface, left and porous surface, right), 5.0-caliber tangent-ogive forebody from USM3Dns: $M_\infty = 0.2$, $\alpha = 30$ deg, and $Re_D = 0.4 \times 10^5$.

the porous boundary condition. Because surface porosity restores flow symmetry, most of the following assessments will be performed on symmetric half-plane grids. One full-body asymmetric flow solution is included for completeness.

Both structured-hexahedral and unstructured-tetrahedral grids were constructed for the study. The structured grid for TLNS3D and CFL3D contained $177 \times 97 \times 65$ cells, and the unstructured grid for USM3Dns had 1,009,929 cells. The USM3Dns grid is mirrored for the full body computation. Farfield boundaries were placed at $x_{\min}$, $y_{\min}$, and $z_{\min}$ of −120, 0, and −150 in. (−304·8, 0, 381 cm) and $x_{\max}$, $y_{\max}$, and $z_{\max}$ of 40, 180, and 150 in. (101.6, 457.2, 381 cm), respectively. A characteristic inflow/outflow boundary condition was applied to the inflow, top, and side boundaries. An outflow extrapolation condition was prescribed to the aft boundary. The no-slip condition was applied to the solid surfaces on the ogive, with the exception that USM3Dns utilized a wall function. A 22% porosity ($s = 0{\cdot}78$) boundary condition is applied to the darkened forebody surface region denoted in Fig. 4.

Navier–Stokes solutions were computed on the ogive body with the three flow codes at $M_\infty = 0{\cdot}2$, $\alpha = 30$ and 40 deg, and $Re_D = 4 \times 10^5$. TLNS3D and USM3Dns utilized the Spalart–Allmaras one-equation turbulence model and CFL3D the Menter SST two-equation model. The solid surface solutions were computed first. Then the porous boundary condition was activated and the solutions restarted. Figure 5 presents the typical convergence of the surface net mass flux and the plenum and surface-averaged pressures for the porous region after restarting from a converged solid-surface solution. Note that the plenum pressure is substantially different than the surface-averaged value. Earlier studies assessed the use of surface-averaged pressure as the plenum pressure with the porosity boundary condition. This approach was determined to yield inaccurate results, which led to the development of the iterative procedure for plenum pressure that was described earlier. For the results presented herein, the values for plenum pressure were determined from the USM3Dns solutions and provided as input for the other codes. The final nondimensional plenum pressures for $\alpha = 30$ and 40 deg were 0.7118 and 0.7099, respectively, where nondimensional freestream pressure is 0.7143.

The effect of porosity on the offbody flowfield is evident in Fig. 6. Contours of density are shown at station $x = 10$ in. (25.4 cm) ($x/D = 2{\cdot}5$) for $\alpha = 30$ deg for the solid-surface solution (left) and porous-surface solution (right). The tightly clustered contour lines over the solid surface denote the presence of a strong vortex core, whereas the lines over the porous surface suggest a more diffused vortical system.

A comparison of surface circumferential C_p distributions is shown in Figs. 7 and 8 at $x = 10$ in. (25.4 cm) ($x/D = 2{\cdot}5$) for angles of attack of 30 and 40 deg, respectively. A strong asymmetry is evident in the experimental distributions for the solid surface, which is the source of unwanted load asymmetries on the ogive. The beneficial effect of passive porosity is evidenced in the companion experimental data by a diffusion of the vortex suction peaks into a symmetric distribution.

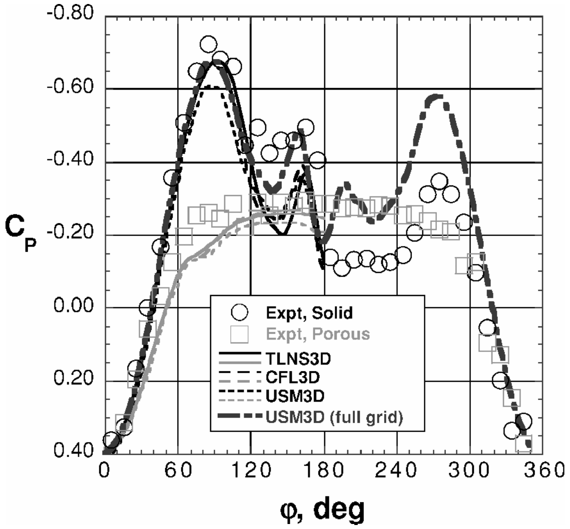

Fig. 7 Code to code comparison of circumferential C_p distribution on 5.0-caliber tangent-ogive forebody with and without porosity: station $x/D = 2.5$, $M_\infty = 0.2$, $\alpha = 30$ deg, and $Re_D = 4 \times 10^5$.

A full-grid solution from USM3Dns is included in Figs. 7 and 8 to illustrate the difficulty of computing accurate surface pressure distributions with a solid (nonporous) surface for this class of problem. Note that asymmetric solutions are produced, but that the accuracy is relatively poor. These solutions were generated at zero sideslip with an initial asymmetry triggered by application of asymmetric viscous boundary conditions on the nose upstream of $x = 1$ in. (2.54 cm) a wall function on the starboard side, and a no-slip condition on the port side. Subsequent porous computations (not shown) were restarted from the asymmetric solutions. Flow symmetry was restored even with the asymmetric viscous boundary conditions set ahead of $x = 1$ in. (2.54 cm).

The computational C_p distributions on the half-plane grids are presented in Figs. 7 and 8 between $\varphi = 0$ and 180 deg. The distributions from the solid (nonporous) solutions are included to facilitate code-to-code comparisons and are not intended to reflect a correct solution to an inherently asymmetric problem. Some

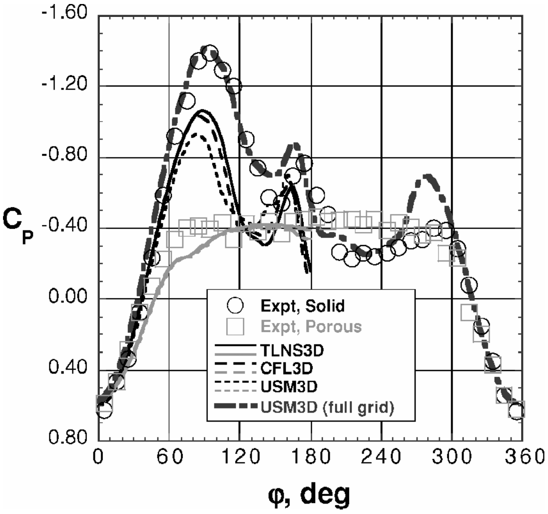

Fig. 8 Code to code comparison of circumferential C_p distribution on 5.0-caliber tangent-ogive forebody with and without porosity: station $x/D = 2.5, M_\infty = 0.2, \alpha = 40$ deg, and $Re_D = 4 \times 10^5$.

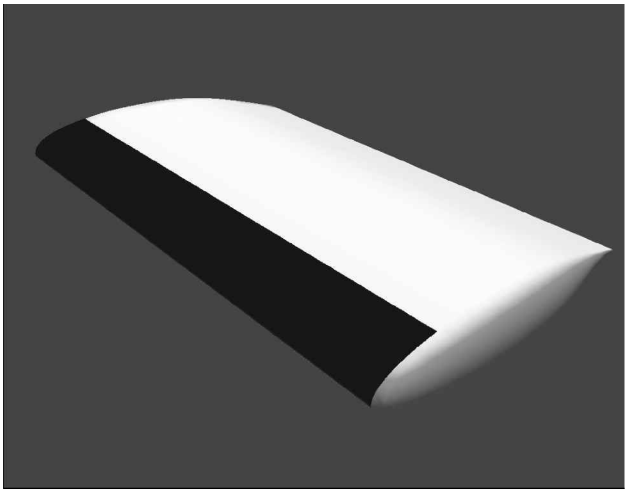

Fig. 9 Semispan surface geometry for GA(W)-1 wing; porosity applied to shaded region around leading edge.

differences in C_p distribution are noted between codes, but each qualitatively captures the dominant vortex flow features. The focus is on the porous surface results that demonstrate good quantitative agreement with the experimental data. This confirms the adequacy of the new porous surface boundary condition for the computation of aggregate aerodynamic effects of passive porosity for this class of problem.

GA(W)-1 Wing

The GA(W)-1 wing was tested in the 14- by 22-Foot Subsonic Wind Tunnel. This model had a 9-ft (2.74 m) span, 3-ft (0.914 m) chord, and 0-deg leading-edge sweep. Surface pressure taps were located at three spanwise locations. The model was also equipped with porous skins to represent a passive porous test article (porous surface with plenum cavity).

The semispan surface definition used for the computations is shown in Fig. 9. Porosity was applied to the shaded leading-edge region ahead of the 18% chord station. Computational grids were constructed for each of the flow solvers. The grid for TLNS3D and CFL3D contained 193 × 65 × 33 hexahedral cells, whereas for USM3Dns, the grid contained 1,681,831 tetrahedral cells. Farfield boundaries were placed 10 chord lengths away from the wing in all directions at which a characteristic inflow/outflow boundary condition was applied. The no slip condition was applied to the wing solid surfaces, with the exception that USM3Dns utilized a wall function. When the leading-edge porosity was applied, a 22% condition ($s = 0{\cdot}78$) was prescribed to the darkened region denoted in Fig. 9.

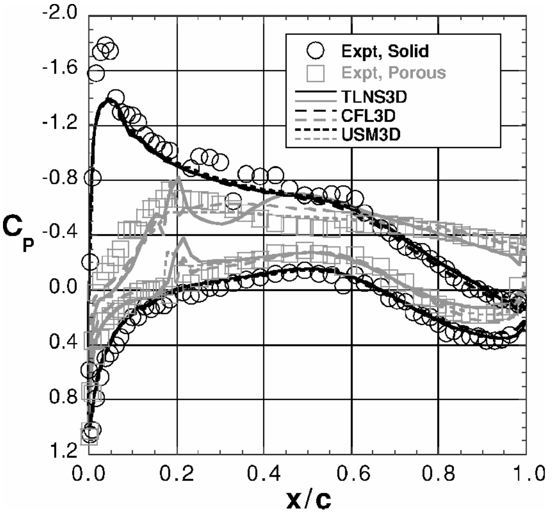

Fig. 10 C_p comparison of solid and porous GA(W)-1 wing for TLNS3D and USM3Dns with experiment at $2y/b = 0.67$: $M_\infty = 0.17, \alpha = 8$ deg, and $Re_c = 3.5 \times 10^6$

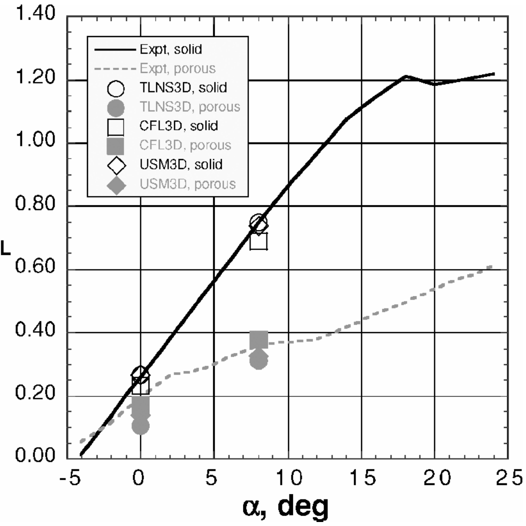

Fig. 11 Comparison of lift characteristics of solid and porous leading edge for GA(W)-1 wing: $M_\infty = 0.17$ and $Re_c = 3.5 \times 10^6$.

Navier–Stokes flow solutions were computed at $M_\infty = 0{\cdot}17$, $\alpha = 0$ and 8 deg, and a chord Reynolds number of $3{\cdot}5 \times 10^6$. As before, the plenum pressure was determined from USM3Dns and provided as input for the other codes. The nondimensional plenum values used for $\alpha = 0$ and 8 deg were 0.7130 and 0.7156, respectively.

Figure 10 compares the chordwise C_p distributions at $\alpha = 8$ deg and $2y/b = 0{\cdot}67$ (one chord length from the symmetry plane) between the code results and experimental data for the solid and porous surfaces. The experimental data reveal a dramatic loss of leading-edge suction peak and consequent loss of lift due to passive porosity. The solid surface computational results are nearly identical between the codes and are in generally good agreement with the experimental data, with the exception of the leading-edge suction peak. The porous leading-edge computations show some variation between codes, but are in reasonably good agreement with the data.

Figures 11 and 12 illustrate the large impact of leading-edge porosity on lift and drag coefficients and demonstrate that the porosity boundary condition model yields correct estimates of those effects at angles of attack of 0 and 8 deg. With leading-edge porosity inducing such a large effect on lift and drag, an asymmetric application of this device could be envisioned for lateral-directional control

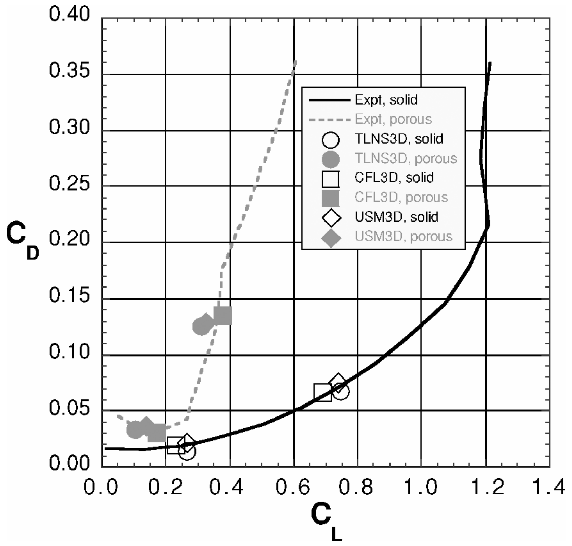

Fig. 12 Comparison of drag characteristics of solid and porous leading edge for GA(W)-1 wing: $M_\infty = 0.17$ and $Re_c = 3.5 \times 10^6$.

in place of moving control surfaces. The computational model presented herein should be useful as a supplemental design tool in what was previously an intensive experimental process.

Conclusions

A new boundary condition is presented for simulating the flow over porous surfaces. The model builds on the earlier work of Bush[21] to eliminate the need for constructing a grid within an underlying plenum, thereby simplifying the numerical modeling of passively porous flow control systems and reducing computation cost.

Code experts for two structured-grid flow solvers, TLNS3D and CFL3D, and one unstructured solver, USM3Dns, collaborated with an experimental porosity expert to develop the model and implement it into their respective codes. Results presented for the three codes on a slender forebody with porosity, and a wing with leading-edge porosity, demonstrate good agreement with experimental data and a remarkable ability to predict the aggregate aerodynamic effects of surface porosity with a simple boundary condition.

Experimental studies of surface porosity have shown the strong potential for this technology as a flow control device. Porosity has many potential applications for aerodynamic control, drag reduction/production, separation control, and lift improvement. The present work should facilitate a more complete understanding of surface porosity in the future by enabling complementary computational studies and more timely design trade analysis.

References

[1] Hunter, C. A., Viken, S. A., Wood, R. M., and Bauer, S. X. S., "Advanced Aerodynamic Design of Passive Porosity Control Effectors," AIAA Paper 2001-0249, Jan. 2001.

[2] Thiede, P., Krogmann, P., and Stanewsky, E., "Active and Passive Shock/Boundary Layer Interaction Control on Supercritical Airfoils," *Proceedings of the 365th AGARD-Conference Improvement of Aerodynamic Performance Through Boundary Layer Control and High Lift Systems*, Brussels, Belgium, Paper 24, May 1984.

[3] Bahi, L., and Ross, J. M., "Passive Shock Wave/Boundary Layer Control for Transonic Airfoil Drag Reduction," AIAA Paper 83-0137, Jan. 1983.

[4] Savu, G., Trifu, O., and Dumitrescu, L. Z., "Suppression of Shocks on Transonic Airfoils," Sydney Shock Tube Symposium Publishers, Sydney, Australia, Aug. 1984, pp. 92–101.

[5] Savu, G., and Trifu, O., "Porous Airfoils in Transonic Flow," *AIAA Journal*, Vol. 22, No. 7, 1984, pp. 989–991.

[6] Nagamatsu, H. T., and Orozco, R. D., "Porosity Effect on Supercritical Airfoil Drag Reduction by Shock Wave/Boundary Layer Control," AIAA Paper 84-1682, June 1984.

[7] Bauer, S. X. S., and Hernandez, G., "Reduction of Cross-Flow Shock-Induced Separation with a Porous Cavity at Supersonic Speeds," AIAA Paper 88-2567, June 1988.

[8] Wood, R. M., Banks, D. W., and Bauer, S. X. S., "Assessment of Passive Porosity with Free and Fixed Separation on a Tangent–Ogive Forebody," AIAA Paper 92-4494, Aug. 1992.

[9] Bauer, S. X. S., and Hemsch, M. J., "Alleviation of Side Force on Tangent–Ogive Forebodies Using Passive Porosity," *Journal of Aircraft*, Vol. 31, No. 2, 1993, pp. 354–361.

[10] Allen, H. J., and Perkins, E. W., "A Study of the Effects of Viscosity on Flow Over Slender Inclined Bodies of Revolution," NACA TR 1048, Dec. 1951.

[11] Letko, W., "A Low-Speed Experimental Study of the Directional Characteristics of a Sharp Nosed Fuselage Through a Large Angle-of-Attack Range at Zero Angle of Sideslip," NACA TN 2911, July 1953.

[12] Coe, Jr., P. L., Chambers, J. R., and Letko, W., "Asymmetric Lateral-Directional Characteristics of Pointed Bodies of Revolution at High Angles of Attack," NASA TN D 7095, Nov. 1972.

[13] Pick, G. S., "Investigation of Side Forces on Ogive–Cylinder Bodies at High Angles of Attack in the M _ 0·5 to 1.1 Range," AIAA Paper 71-570, June 1971.

[14] Clark, W. H., and Peoples, J. R., "Occurrence and Inhibition of Large Yawing Moments During High Incidence Flight of Slender Missile Configurations," AIAA Paper 72-968, Sept. 1972.

[15] Jorgensen, L. H., and Nelson, E. R., "Experimental Aerodynamic Characteristics for a Cylindrical Body of Revolution with Various Noses at Angles of Attack from 0° to 58° and Mach Numbers from 0.6 to 2.0," NASA TM X-3128, Dec. 1974.

[16] Jorgensen, L. H., and Nelson, E. R., "Experimental Aerodynamic Characteristics for a Cylindrical Body of Revolution with Side Strakes and Various Noses at Angles of Attack from 0° to 58° and Mach Numbers from 0.6 to 2.0," NASA TM X-3130, March 1975.

[17] Jorgensen, L. H., and Nelson, E. R., "Experimental Aerodynamic Characteristics for Bodies of Elliptic Cross Section at Angles of Attack from 0° to 58° and Mach Numbers from 0.6 to 2.0," NASA TM X-3129, Feb. 1975.

[18] Morgan, H. L., Jr., and Paulson, J. W., Jr., "Aerodynamic Characteristics of Wing–Body Configuration with Two Advanced General Aviation Airfoil Sections and Simple Flap Systems," NASA TN D-8524, Aug. 1977.

[19] Hartwich, P. M., "Euler Study on Porous Transonic Airfoils with a View Toward Multipoint Design," *Journal of Aircraft*, Vol. 30, No. 2, 1993, pp. 184–191.

[20] Kraushaar, S. L., and Chokani, N., "Improved Models for the Porous Surface with Passive Control," M.S. Thesis, North Carolina State Univ., Raleigh, NC, 1996.

[21] Bush, R. H., "Engine Face and Screen Loss Models for CFD Applications," AIAA Paper 97-2076, June 1997.

[22] Cornell, W. G., "Losses in Flow Normal to Plane Screens," *Transactions of the ASME*, Vol. 80, May 1958, pp. 791–799.

[23] Rouse, H., "Elementary Mechanics of Fluids," Dover, New York, 1946/1978, p. 57.

[24] Vatsa, V. N., and Wedan, B. W., "Development of a Multigrid Code for 3-D Navier–Stokes Equations and Its Application to a Grid-Refinement Study," *Computers and Fluids*, Vol. 18, No. 4, 1990, pp. 391–403.

[25] Vatsa, V. N., Sanetrik, M. D., and Parlette, E. B., "Development of a Flexible and Efficient Multigrid-Based Multiblock Flow Solver," AIAA Paper 93-0677, Jan. 1993.

[26] Krist, S. L., Biedron, R. T., and Rumsey, C. L., "CFL3D User's Manual (Version 5.0)," NASA/TM-1998-208444, 1998.

[27] Roe, P. L., "Approximate Riemann Solvers, Parameter Vectors, and Difference Schemes," *Journal of Computational Physics*, Vol. 43, No. 2, 1981, pp. 357–372.

[28] Van Leer, B., "Flux Vector Splitting for the Euler Equations," *Lecture Notes in Physics*, Vol. 170, June–July 1982, pp. 501–512.

[29] Menter, F. R., "Two-Equation Eddy-Viscosity Turbulence Models for Engineering Applications," *AIAA Journal*, Vol. 32, No. 8, 1994, pp. 1598–1605.

[30] Frink, N., "Tetrahedral Unstructured Navier–Stokes Method for Turbulent Flows," *AIAA Journal*, Vol. 36, No. 11, 1998, pp. 1975–1982.

[31] Spalart, P. R., and Allmaras, S. R., "A One-Equation Turbulence Model for Aerodynamic Flows," AIAA Paper 92-0439, 1992.

[32] Hartwich, P. M., and Hall, R. M., "Navier–Stokes Solutions for Vortical Flows over a Tangent Ogive Cylinder," *AIAA Journal*, Vol. 28, No. 7, 1990, pp. 1171–1179.

[33] Hartwich, P. M., Hall, R. M., and Hemsch, M. J., "Navier–Stokes Computations of Vortex Asymmetries Controlled by Small Surface Imperfections," *Journal of Spacecraft and Rockets*, Vol. 28, No. 2, 1991, pp. 258–264.